Periodic folding of a falling viscoelastic sheet

Kui Pan, A. Srikantha Phani,[*] and Sheldon Green

Department of Mechanical Engineering, University of British Columbia, Vancouver, British Columbia V6T 1Z4, Canada

A viscoelastic solid sheet fed from a certain height towards a rigid horizontal plane folds on itself provided that there is no slip. This phenomenon commonly occurs in the manufacturing process of textile and paper products. In this paper we apply a particle dynamics model to investigate this phenomenon. At a low feeding velocity and low viscosity, the inertial effect and the viscous dissipation within the sheet are negligible, and our model successfully reproduces the existing quasistatic results in the gravitational regime. As the feeding velocity and the viscosity of the sheet increase, the folding process changes significantly. The length of the folds decrease and the "rolling back" motion of the sheet vanishes. In the inertial regime, a scaling law between the fold length and the feeding velocity is derived by balancing the kinetic energy and the elastic bending energy involved in folding, which is verified by the simulation. It is found that above a critical feeding velocity, the folding morphology transforms from line contact into point contact with the sheet exhibiting a lemniscate-like pattern. Finally, a phase diagram for the folding morphology is constructed. The results presented in this work may offer some insights into the high-speed manufacturing of paper and fabric sheets.

I. INTRODUCTION

When slender objects such as ropes, filaments, and sheets are fed from a sufficient height towards a horizontal plane, instability usually occurs, which gives rise to a series of intriguing phenomena including periodic folding and coiling [1–15]. Periodic folding is typically associated with sheet-type objects [1–9] and the deformation is two-dimensional, while coiling happens with ropes and filaments [10–15] where deformation is three-dimensional and twisting is essential. Both folding and coiling occur in a variety of materials whose rheology ranges from purely elastic to purely viscous. For viscous coiling, four distinct regimes (viscous, gravitational, inertio-gravitational, and inertial) have been identified as the normalized falling height increases [12]. For elastic coiling, three basic regimes (elastic, gravitational, and inertial) exist depending on the relative magnitude of various energies, and in the inertial regime there are two distinct modes: "whirling string" and "whirling shaft" [15]. More complex coiling patterns have been revealed when the rope falls on a horizontal moving belt, which is known as a "sewing machine" [16–22]. Similar to coiling, periodic folding is also governed by the interplay between various energies. For example, for viscous sheets under the assumption that the fluid inertia is negligible, the viscous force can be balanced by the gravity, which leads to a viscogravitational folding length as $l_f^{vg} \sim (\mu I V_0 / \rho h w g)^{1/4}$, where μ, I, V_0, ρ, h, w, and g represent the dynamic viscosity, second moment of area of the sheet cross section, feeding velocity, density, thickness, width, and gravity, respectively [1]. It is worth mentioning that a leading-order logarithmic term can be present in the expression for the aforementioned viscogravitational folding

length in the gravitational regime, when the upper part of the sheet behaves like a hanging catenary [21,22]. However, for the folding of a viscoelastic paper sheet that we are going to investigate in this paper, the logarithmic term varies very little and thus can be neglected. For elastic sheets, when the feeding velocity of the material is low (quasistatic case), only the gravitational energy and the elastic bending energy of the sheet are important [4]. Balancing these two energies leads to a gravito-bending folding length as $l_f^{gb} \sim (EI/\rho h w g)^{1/3}$ with E being the Young's modulus [4,6]. However, as the feeding velocity increases, the kinetic energy of the sheet becomes comparable with the gravitational energy, and thus the inertia cannot be neglected. Although the coiling phenomenon of ropes (filaments) in the inertial regime has been well explored [10–22], the inertial effect on the folding of thin sheets remains unclear. Furthermore, only purely elastic or purely viscous materials have been considered to our knowledge. For viscoelastic sheets, elasticity and viscosity can simultaneously affect the folding process. Motivated by this, in this paper we study the periodic folding of a falling viscoelastic sheet with a special interest in the inertial regime. In order to consider the in-plane viscous dissipation, the extensibility of the sheet is also accounted for.

An example of the periodic folding of a viscoelastic sheet can occur in the manufacturing process of paper products, during which a paper sheet is fed from a spool towards a horizontal solid plane below it, forming a series of folds. In a typical paper machine, the feeding speed can reach around 30 m/s and paper is essentially a viscoelastic material [23]. Due to the nonlinearity of the governing equations and the complex boundary condition, the analytical solution of this problem is impossible. Here we propose to use a particle dynamics model to simulate the folding process and combine the simulation with an approximate energy analysis. Particle-based methods have been widely used in applied

----
[*]Corresponding author: skpa@mail.ubc.ca
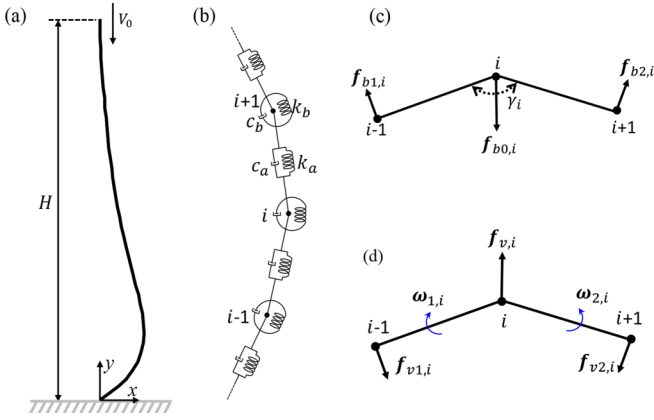
FIG. 1. (a) Edge-on view of a buckled thin viscoelastic sheet when it touches ground. V_0 and H represent the feeding velocity and feeding height, respectively. (b) Schematic of the particle system: k_a represents the axial stiffness; k_b represents the stiffness of the rotational spring; c_a represents the axial damping coefficient; c_b represents the rotational damping coefficient. (c) Schematic of elastic bending forces in the local bending system formed by particles $(i-1) - (i) - (i+1)$. (d) Schematic of viscous bending forces: $f_{v1,i}$ is due to the angular velocity $\omega_{1,i}$, $f_{v2,i}$ is due to the angular velocity $\omega_{2,i}$, and $f_{v,i}$ is the negative sum of $f_{v1,i}$ and $f_{v2,i}$.

mechanics over the past few decades. In particle-based models, the material is treated as a series of discrete particles (masses) and the connections between neighboring particles are determined by constitutive equations [24–28]. Significant developments of the particle-based approach have been made, such as the meshfree Galerkin methods, the smoothed particle hydrodynamics, and the popular molecular dynamics, reviewed in detail in Ref. [29]. Recently a particle dynamics model has been applied to simulate the dynamics of the paper web running in the open-draw section [30] and the periodic buckle-delamination in the "creeping" process of tissue making [31,32]. The sheet is treated as a series of discrete masses connected by viscoelastic (Kelvin-Voigt) elements which can capture the large deformation and the viscoelasticity. In this paper we use this particle approach to investigate the periodic folding of a viscoelastic sheet.

The remainder of this paper is organized as follows. In Sec. II the discrete particle model is presented. In Sec. III the model is applied to simulate the folding process of a viscoelastic sheet. First, the quasistatic results are reproduced. Then the effects of inertia and viscosity are discussed in the dynamic case. Section IV summarizes the main conclusions drawn from this study.

II. THEORETICAL MODEL

Figure 1(a) shows a falling viscoelastic solid sheet as it starts to buckle following contact with a steady horizontal plane due to the compression. Note the choice of the Kelvin-Voigt model given our interest in textile and paper-folding processes. V_0 and H represent the vertical feeding velocity and feeding height. To simulate the folding process, the model needs to capture the large buckling deformation and the contact between the sheet and the ground.

A. Particle approach

We assume that deformation along the width direction is uniform during folding of the sheet, thus twisting can be neglected. The sheet can be modeled as a series of discrete particles connected by axial and rotational viscoelastic elements, shown as Fig. 1(b). The axial spring-damper element known as the Kelvin-Voigt model has been shown to be suitable to model the viscoelasticity of paper products [33]. $a_0 = L_0/(N-1)$ and $m = \rho h a_0 w$ are the spacing and mass of the particles, respectively, where L_0, w, ρ, and h represent the initial length, width, density, and thickness of the web, respectively, and N denotes the total number of particles. The axial stiffness is given by $k_a = Ewh/a_0$ where E is Young's modulus. After deformation the axial elastic force acting on particle i in vector form is

$$f_{a,i} = k_a(|r_{i-1} - r_i| - a_0)e_{i,i-1} + k_a(|r_{i+1} - r_i| - a_0)e_{i,i+1},$$ (1)

where $e_{i,i+1}$ denotes a unit vector pointing from particle i to particle $i+1$ and r_i is the position vector of particle i. The notation $|r|$ is used to represent the magnitude of the vector r. Since the extensibility of the sheet is considered in this paper, the in-plane viscous dissipation needs to be considered. The in-plane viscous force is related to the axial velocity difference between two adjacent particles:

$$f_{d,i} = -c_a[(\dot{r}_i - \dot{r}_{i-1}) \cdot e_{i,i-1}]e_{i,i-1} - c_a[(\dot{r}_i - \dot{r}_{i+1}) \cdot e_{i,i+1}]e_{i,i+1},$$ (2)

where $\dot{r}_i$ represents the velocity of particle i and c_a denotes the phenomenological viscous damping coefficient with $c_a = \mu wh/a_0$. Here μ is the dynamic viscosity of the sheet.

Since the particles are not endowed with a rotational degree of freedom, we cannot directly apply the bending moment. Instead, we introduce bending forces to the particles to achieve the same bending effect. We consider a local bending system formed by three consecutive particles $(i-1)$, (i), and $(i+1)$, as shown in Fig. 1(c). Due to the bending effects, the system tends to recover to the initial flat state. Thus, we can imagine there are two restoring forces $f_{b1,i}$ and $f_{b2,i}$ acting on the left particle $(i-1)$ and the right particle $(i+1)$ to achieve that effect. The restoring forces are perpendicular to the axial direction and related to the local bending angle γ_i, given by [30]

$$|f_{b1,i}| = |f_{b2,i}| = \frac{k_b(\gamma_0 - \gamma_i)}{a_0^2(1 + \varepsilon_i)^2},$$ (3)

where $k_b = Ewh^3/12$ is the bending stiffness, $\gamma_0 = \pi$ is the initial bending angle, and $\varepsilon_i = (|r_{i+1} - r_i| - a_0)/a_0$ is the axial strain. Equation (3) can also be derived by taking the gradients of the system's total bending energy [7]. Since the restoring forces are internal forces, in order to maintain the overall bending force equilibrium, a force is applied on the central particle i, given by $f_{b0,i} = -f_{b1,i} - f_{b2,i}$. Note that $f_{b0,i}$ applied on particle i is only corresponding to the bending system $(i-1) - (i) - (i+1)$. Particle i is also subject to the restoring force $f_{b2,i-1}$ due to the bending system

$(i-2) - (i-1) - (i)$, and $\boldsymbol{f}_{b1,i+1}$ due to the bending system $(i) - (i+1) - (i+2)$. Thus, the total elastic bending force acting on particle i is

$$\boldsymbol{f}_{b,i} = \boldsymbol{f}_{b0,i} + \boldsymbol{f}_{b2,i-1} + \boldsymbol{f}_{b1,i+1}. \tag{4}$$

During buckling, as the local bending angle γ_i changes, the sheet is also subject to viscous dissipation that slows down this process. The viscous bending moment is proportional to $\dot{\gamma}_i$ and can be derived as $\mu \dot{\gamma}_i w h^3 / 12 a_0$. The detailed derivation can be found in Appendix A. We implement the viscous bending moment in a similar fashion as the elastic bending moment, by introducing the corresponding viscous forces as shown in Fig. 1(d). The magnitude of the viscous bending force can be written as

$$|\boldsymbol{f}_{v1,i}| = |\boldsymbol{f}_{v2,i}| = \frac{c_a \dot{\gamma}_i h^2}{12 a_0}, \tag{5}$$

where $c_a = \mu w h / a_0$ is the phenomenological damping coefficient. $\boldsymbol{f}_{v1,i}$ and $\boldsymbol{f}_{v2,i}$ are perpendicular to the segments $(i-1) - (i)$ and $(i) - (i+1)$ respectively, and the exact directions depend on whether the local bending angle γ_i is increasing or decreasing. For example, in Fig. 1(d) γ_i is increasing, so $\boldsymbol{f}_{v1,i}$ and $\boldsymbol{f}_{v2,i}$ both point "inward" and slow down the increase of γ_i. In a discrete particle system, $\dot{\gamma}_i$ is related to the angular velocities $\boldsymbol{\omega}_{1,i}$ and $\boldsymbol{\omega}_{2,i}$ as $\dot{\gamma}_i = \boldsymbol{\omega}_{1,i} - \boldsymbol{\omega}_{2,i}$. Here $\boldsymbol{\omega}_{1,i}$ can be calculated based on the velocity difference between the particle $i-1$ and the particle i and on the length of the segment $(i-1) - (i)$. $\boldsymbol{\omega}_{2,i}$ can be derived following the same rule. When $\boldsymbol{\omega}_{1,i}$ is equal to $\boldsymbol{\omega}_{2,i}$, $\dot{\gamma}_i$ becomes zero and the sheet undergoes rigid rotation. As before, to maintain the overall force balance, we apply a viscous bending force applied on particle i, given by $\boldsymbol{f}_{v,i} = -\boldsymbol{f}_{v1,i} - \boldsymbol{f}_{v2,i}$.

B. Contact model

We model the contact between the sheet and the horizontal plane based on a penalty method. The contact force applied on the particle i is given by

$$|\boldsymbol{f}_{c,i}| = \begin{cases} k_c |y_i|, & y_i < 0 \\ 0, & y_i \geqslant 0 \end{cases}, \tag{6}$$

where k_c is the contact stiffness. To prevent any significant penetration of the sheet into the ground, k_c is chosen three orders larger than the axial stiffness of the sheet. Based on the Coulomb friction law the friction force applied on the particle i is given by $|\boldsymbol{f}_{f,i}| \leqslant \mu_f |\boldsymbol{f}_{c,i}|$, where μ_f is the friction coefficient. Although it is reported that slipping between the sheet and the horizontal plane can result in different folding morphologies [7], in this paper we focus on the effects of inertia and viscosity. Throughout the paper, μ_f is fixed as 1 to prevent slipping of the sheet.

C. Numerical implementation

We start our simulation when the sheet first touches the rigid horizontal plane at time $t = 0$. Initially the total length of the sheet equals the feeding height H, and the sheet is discretized into N particles with $a_0 = H/(N-1)$. The initial speed for all particles equals the feeding speed. We always fix the velocity of the last particle in the system as the feeding

velocity V_0, and when its distance from the feeding point reaches a_0 we feed a new particle into the system. Then this new particle becomes the last particle in the system. This will ensure the boundary condition at the feeding point is consistent throughout the simulation. Once the particles hit the ground, we did not remove them from the system. Instead, we let them relax on their own to reach the equilibrium. Since we are not considering the self-contact between the folds, the presence of the fold does not affect the development of the subsequent folds.

The total force applied on the particle i includes the axial elastic force $\boldsymbol{f}_{a,i}$, the axial viscous damping force $\boldsymbol{f}_{d,i}$, the elastic bending force $\boldsymbol{f}_{b,i}$, the viscous bending force $\boldsymbol{f}_{v,i}$, the contact force by the ground $\boldsymbol{f}_{c,i}$, the friction force $\boldsymbol{f}_{f,i}$, and the gravity $m\boldsymbol{g}$. We evolve the particle system according to Newton's equation of motion:

$$\boldsymbol{f}_{\text{tot},i} = \boldsymbol{f}_{a,i} + \boldsymbol{f}_{d,i} + \boldsymbol{f}_{b,i} + \boldsymbol{f}_{v,i} + \boldsymbol{f}_{c,i} + \boldsymbol{f}_{f,i} + m\boldsymbol{g} = m\ddot{\boldsymbol{r}}_i. \tag{7}$$

The "semi-implicit" Euler method is adopted for the advancement in time [34]. Given the particle's position vector $\boldsymbol{r}_i^t$ and velocity $\dot{\boldsymbol{r}}_i^t$ at time t, the total force $\boldsymbol{f}_{\text{tot},i}^t$ applied on the particle i can be calculated, which gives the acceleration $\ddot{\boldsymbol{r}}_i^t = \boldsymbol{f}_{\text{tot},i}^t / m$. Then the particle's velocity and position at time $t + \Delta t$ can be updated:

$$\dot{\boldsymbol{r}}_i^{t+\Delta t} = \dot{\boldsymbol{r}}_i^t (1 - \lambda) + \ddot{\boldsymbol{r}}_i^t \Delta t, \tag{8}$$

$$\boldsymbol{r}_i^{t+\Delta t} = \boldsymbol{r}_i^t + \dot{\boldsymbol{r}}_i^{t+\Delta t} \Delta t, \tag{9}$$

where Δt is the time step and λ is a numerical damping coefficient that can be applied to improve numerical stability, if we are only interested in the final equilibrium state of the system. The elastic bending model and the viscous damping model are both validated in Appendix B and Appendix C, respectively.

III. RESULTS AND DISCUSSION

A. Energy analysis

Considering a fold with an arc length l_f formed as the falling viscoelastic sheet hits the ground, before folding the initial kinetic energy scales as $\rho h w l_f V_0^2$ and the gravitational potential energy scales as $\rho g h w l_f^2$. Due to the viscous effect and extensibility of the sheet, the folding process is associated with both bending and in-plane stretching dissipations, represented by the axial and rotational dampers in Fig. 1(b). The axial stress caused by the bending dissipation is proportional to the strain rate, given by $\sigma \sim \mu(z\phi_s)_t \sim \mu z \phi_{st}$. Here z represents the distance to the midplane in the cross-direction and ϕ_s represents the curvature. Integrating $\sigma z dA$ over the cross section and using the approximation $\phi_{st} \sim V_0/l_f^2$, the viscous bending moment can be derived as $M_\mu \sim \int_{-h/2}^{h/2} \sigma z w \, dz \sim \int_{-h/2}^{h/2} \mu z^2 w V_0/l_f^2 dz \sim \mu I V_0/l_f^2$. Finally integrating $M_\mu \phi_s$ along the length of the sheet, the total energy dissipated by viscous bending scales as $\int_0^{l_f} M_\mu \phi_s ds \sim \int_0^{l_f} M_\mu/l_f ds \sim \mu I V_0/l_f^2$. Similarly, we can find the in-plane stretching dissipation scales as $\mu h w \sqrt{g l_f}$. After the folding is completed, the bending energy stored in the sheet scales as

TABLE I. Physical properties of paper sheet [30,32].

Parameter	Value range
E (MPa)	100–600
h (μm)	50–150
ρ (kg/m^3)	250–500
μ (kg/ms)	500–2000
V_0 (m/s)	5–25

$\int_0^{l_f} EI\phi_s^2 ds \sim EI/l_f$. The ratio of the viscous bending energy and the elastic bending energy ($\mu V_0/El_f$) can be interpreted as a ratio of the viscoelastic relaxation time (μ/E) and the time required for a single fold to form (l_f/V_0). This ratio remains small for the folding of a viscoelastic solid for the range of parameters in Table I (relevant for a viscoelastic solid). Arguably, the same ratio can be interpreted as a Deborah number for a viscoelastic fluid folding problem. However, the choice of Kelvin-Voigt viscoelastic solid (see Fig. 1) does not apply to a Maxwell fluid, because under a constant applied stress (creep test), a Kelvin-Voigt viscoelastic solid does not exhibit an unbounded strain (characteristic of a fluid), whereas a Maxwell (dashpot and spring in series) viscoelastic fluid does exhibit fluid-like response after the initial elastic response. This distinction between a viscoelastic solid and viscoelastic fluid is worth noting. Due to the energy balance, the sum of the initial gravitational energy and the kinetic energy should be equal to the sum of the dissipated energies and the bending energy of the fold:

$$c_1 \rho ghwl_f^2 + c_2 \rho hwl_f V_0^2 = c_3 \frac{EI}{l_f} + c_4 \frac{\mu I V_0}{l_f^2} + c_5 \mu hw\sqrt{gl_f},$$
(10)

where $c_1 - c_5$ are the coefficients for each term. Normalizing the above equation by the gravitational potential energy leads to

$$1 + \alpha \frac{V_0^2}{gl_f} = \beta \frac{EI}{\rho ghwl_f^3} + \eta \frac{\mu I V_0}{\rho ghwl_f^4} + \chi \frac{\mu}{\rho \sqrt{gl_f^3}},$$
(11)

where α, β, η, and χ are the corresponding coefficients of four dimensionless groups. $\frac{V_0^2}{gl_f}$ is the square of the Froude number that represents the inertia to gravity ratio. $\frac{EI}{\rho ghwl_f^3}$ is the elastic bending to gravity ratio, which implies the gravito-bending length is $l_f^{gb} \sim (EI/\rho ghw)^{1/3}$, corresponding to the fold length of an elastic sheet under a quasistatic condition [4,6]. $\frac{\mu I V_0}{\rho ghwl_f^4}$ represents the ratio between viscous bending and gravity, leading to the viscogravitational length as $l_f^{vg} \sim (\mu I V_0/\rho hwg)^{1/4}$, which prescribes the fold length of a falling viscous fluid in the gravitational regime [1]. Finally, $\frac{\mu}{\rho \sqrt{gl_f^3}}$ represents the ratio between in-plane viscous dissipation and gravity. In the following sections, we first validate the proposed discrete model by comparison with the existing quasistatic results and then increase the feeding velocity to study the dynamic folding of a viscoelastic sheet.
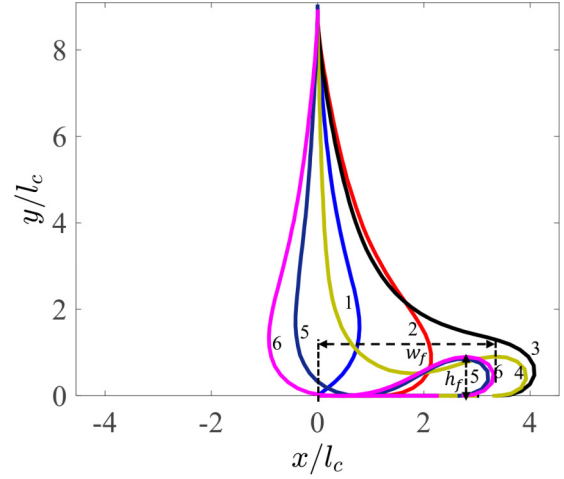
FIG. 2. The equilibrium configurations of the sheet at different stages during the formation of one fold. The falling height is $H = 9l_c$ and feeding velocity is $V_0 = 0.01\sqrt{gH}$. w_f and h_f are defined as the width and the height of the final fold, respectively, corresponding to line 6.

B. Quasistatic case

When the feeding velocity of the sheet is small (i.e., the Froude number is small), the inertial effects can be ignored and the folding process can be analyzed in a quasistatic manner. Under this assumption and based on the inextensible elastica model, Mahadevan and Keller [4] have found that the width and the height of the completely formed fold are $w_f = 3.2324l_c$ and $h_f = 0.9066l_c$, where $l_c = (EI/\rho hwg)^{1/3}$ is the characteristic length (gravito-bending length). w_f and h_f are illustrated in Fig. 2. In our discrete model, the feeding velocity V_0 is set to a small value ($0.01\sqrt{gH}$) to satisfy the quasistatic condition. Since the falling height does not affect the folding process provided that it is much larger than l_c [6], in this paper we fix it as $H = 9l_c$. The numerical damping is chosen as $\lambda = 0.001$, which helps the system to converge to the equilibrium state. Figure 2 shows the evolution of the sheet pattern during the formation of the first fold. When the sheet first touches the horizontal plane it starts buckling, shown as curve 1 in Fig. 2. As the feeding continues, the sheet becomes tangent to the horizontal plane (curve 2) and spreads horizontally to the extreme location, shown as curve 3. After that the sheet starts rolling back towards the feeding plane due to the self-weight of the fold, shown as curve 4. Eventually the sheet touches itself, shown as curve 5. After that, further feeding causes the self-contact line to move back to the feeding plane, and thus one fold is completed, shown as curve 6. Our simulation results (Fig. 2) agree well with the previous studies [4,6]. Based on curve 6 we can measure the fold width and fold height.

Figure 3 shows the width and height of the fold under different values of characteristic length l_c. We can see the relation is linear, and the scaling laws are found as $w_f = 3.35l_c$ and $h_f = 0.904l_c$. The difference between our results and the scaling law given by the inextensible elastica model [4] ($w_f = 3.2324l_c$, $h_f = 0.9066l_c$) is due to the fact that our model accounts for the extensibility of the sheet. Though this difference is not significant, we will show later that
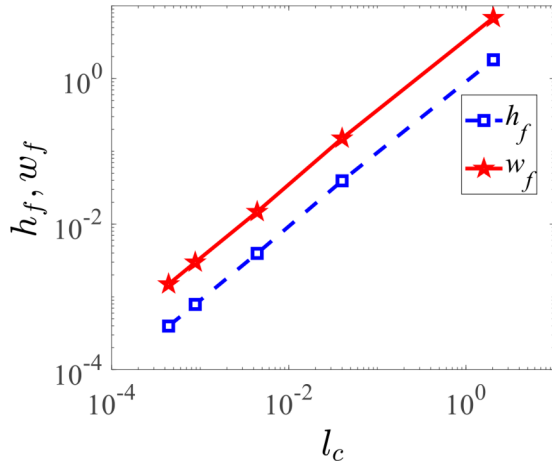
FIG. 3. Simulation results of the fold width w_f (solid line) and fold height h_f (dashed line) as a function of the characteristic length l_c.

in the dynamic folding of a viscoelastic sheet, considering extensibility is important as it allows us to account for the in-plane viscous dissipation, which can significantly affect the folding process.

C. Dynamic case

For dynamic folding simulations, the numerical damping coefficient λ is set to 0 to prevent any artificial dynamic effects. Figure 4 shows the evolution of the sheet morphology during the formation of the first fold. The parameters are chosen as $H = 9l_c$, $V_0/\sqrt{gH} = 0.5$, and $\mu/\mu_* = 2$. μ_* is defined as $\mu_* = \rho\sqrt{gH^3}$ to normalize the dynamic viscosity such that μ/μ_* represents the ratio between in-plane viscous dissipation ($\sim\mu hw\sqrt{g/H}$) and gravity ($\sim\rho ghwH$). Initially the buckling deformation is localized near the horizontal plane, shown as curve 1 and curve 2. As the feeding continues, the sheet starts spreading away from the feeding plane and at
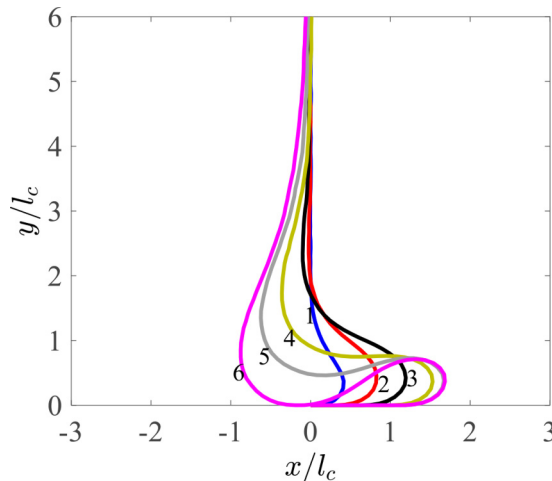
FIG. 4. The evolution of the sheet configuration during the formation of the first fold under dynamic case. The parameters are chosen as $H = 9l_c$, $V_0/\sqrt{gH} = 0.5$ and $\mu/\mu_* = 2$, where μ_* is defined as $\mu_* = \rho\sqrt{gH^3}$.
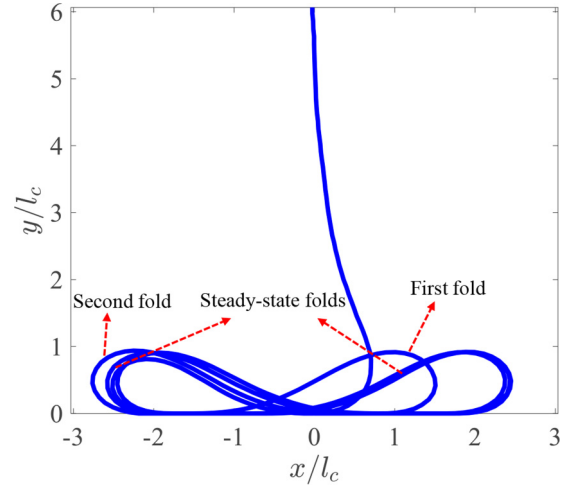
FIG. 5. The configuration of the sheet at steady state after a sufficiently long simulation under the dynamic case. The parameters are the same as in Fig. 4, and the self-contact of the sheet is neglected here.

the same time keeps falling down quickly owing to inertia, as shown in curves 3 to 5. When the buckled sheet contacts the horizontal plane, it stops moving outward due to the friction and a closed fold is formed, shown as curve 6. Unlike the quasistatic case, the sheet does not roll back and the fold width keeps increasing during the folding process. Keep feeding the sheet after the first fold is formed, the subsequent folding process eventually reaches a steady state, and the shape of the fold formed in the steady state remains the same, as shown in Fig. 5. In our simulations the self-contact of the sheet is neglected so the steady-state fold is not affected by the existing folds and depends only on the material properties and dynamics. This approximation is relevant because in practice the existing folded sheet is constantly removed. If desired, self-contact can be embedded into the current discrete model by applying a penalty method [31,32]. Next, we study the effects of the velocity and the viscosity on the size of the steady-state fold.

D. Effects of feeding velocity and viscosity

Table I lists the typical physical properties of paper sheets considered in this study [30,31,33]. Within the given parameter ranges, the viscous bending dissipation is much smaller compared to the elastic bending energy, and the in-plane viscous stretching dissipation on the right-hand of Eq. (11), thus can be neglected. As the feeding velocity increases, the system goes through three different regimes: gravitational, inertio-gravitational, and inertial regimes. In the inertial regime, $\frac{V_0^2}{gl_f}$ becomes much larger than 1. With relatively low viscosity, the in-plane stretching dissipation can also be neglected. Balancing $\frac{V_0^2}{gl_f}$ with $\frac{EI}{\rho ghwl_f^3}$ finally leads to the fold length as

$$l_f \sim \sqrt{\frac{EI}{\rho hw}}\frac{1}{V_0}, \qquad (12)$$
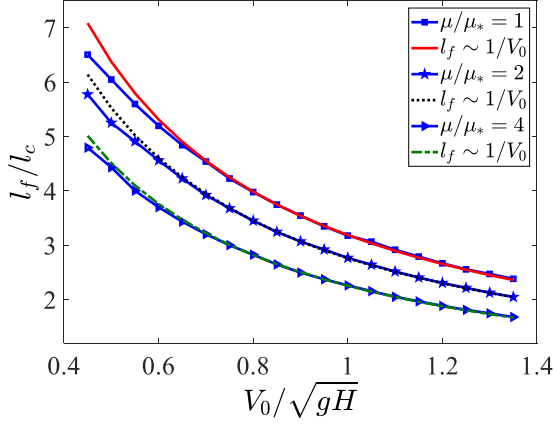
FIG. 6. Normalized fold length l_f/l_c vs normalized velocity $V_0/\sqrt{gH}$ under different viscosity. The solid lines with symbols represent the simulation results, and the dashed lines represent the fitted scaling law.

which suggests that l_f is inversely proportional to V_0 for a given sheet. Noticing that the bending wave speed for a sheet of length l_f equals $\sqrt{EI/\rho hw}/l_f$, this relation also suggests the bending wave effect becomes important in the inertial regime. Figure 6 shows l_f versus V_0 for different viscosities. The solid lines with symbols represent the simulation results, and the other lines represent the scaling law. As V_0 increases the kinetic energy becomes more dominant and the simulation matches very well the scaling law $l_f \sim 1/V_0$ at the high-speed regime. Overall, the folding length decreases as velocity and viscosity increase. The effects of feeding velocity and viscosity can be understood as a competition between the vertical feeding and the horizontal spreading of the sheet during the folding process. Increasing the feeding velocity decreases the time required to form one fold, so the fold has a shorter time to expand horizontally, which eventually results in a smaller fold. On the other hand, increasing the viscosity slows down the deformation process. Within the same amount of time the horizontal distance that the fold can expand becomes shorter, which also results in a smaller fold. Based on the numerical

results of fold length, for each viscosity we can identify a nondimensional coefficient $\varphi(\mu)$ in the inertial regime which satisfies

$$\frac{l_f}{l_c} = \frac{\varphi(\mu)}{V_0/\sqrt{gH}}. \tag{13}$$

E. Fold geometry

From a geometric point of view, the height h_f and the width w_f of the steady-state fold directly depend on the total fold length l_f. Figure 7(a) plots h_f versus l_f, normalized by $l_c = (EI/\rho hwg)^{1/3}$, which is a constant for a given sheet. The discrete symbols representing the simulation results under various velocities and viscosities fall onto one master curve. When l_f is sufficiently large, h_f remains the same value as the quasistatic fold height ($\sim 0.9 l_c$). In this region, we can see from the inserted figure that the fold pattern is similar to the quasistatic fold pattern (shown as Fig. 2, curve 6), and only the width of the fold is decreasing as l_f decreases. However, when l_f is below a critical value $l_{f\_c} = 4.65 l_c$, h_f starts decreasing and the fold morphology changes from "line contact" to "point contact." This transition occurs because the system tries to evolve the configuration to minimize the bending energy of the sheet, for a shorter l_f. The inserted figure shows that the fold transforms into a lemniscate-like pattern and remains geometrically self-similar as l_f keeps decreasing. Away from the transition the curve follows a linear function, defined as

$$\frac{h_f}{l_c} = m\frac{l_f}{l_c} + n, \tag{14}$$

where $m = 0.23$ and $n = 0.05$. Similarly, Fig. 7(b) plots w_f versus l_f. The simulation results also fall into one master curve, which can be described as

$$\frac{w_f}{l_c} = p\frac{l_f}{l_c} + q, \tag{15}$$

where $p = 0.46$ and $q = -0.15$. Figures 7(a) and 7(b) together give the full geometric relations between h_f, w_f, and l_f for the steady-state fold formed in the dynamic process.
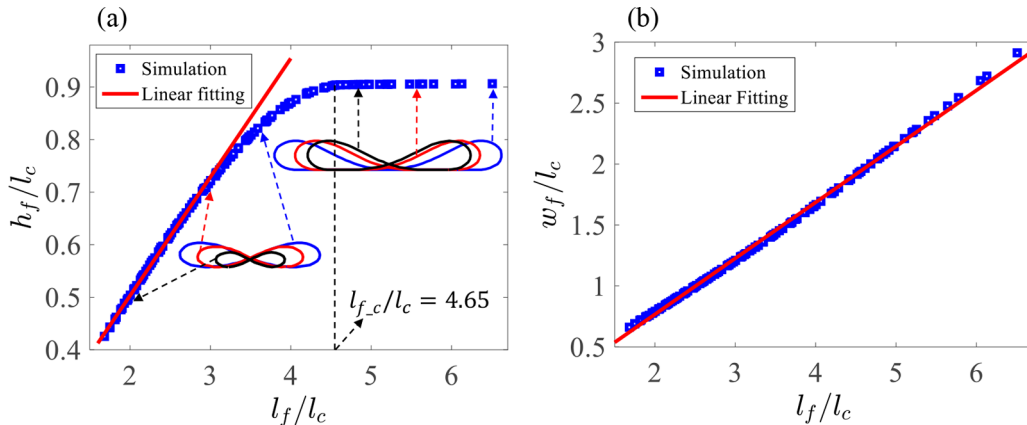
FIG. 7. (a) Normalized fold height h_f/l_c vs. normalized fold length l_f/l_c. l_{f_c} is the critical folding length below which the folding pattern becomes point contact. (b) Normalized fold width w_f/l_c vs normalized fold length l_f/l_c. In both figures the discrete symbols represent the simulation results under various viscosity and velocity. The solid lines are the linear fitting according to Eqs. (13) and (14). The inserted figures in (a) show the steady-state fold patterns at different values of l_f/l_c.
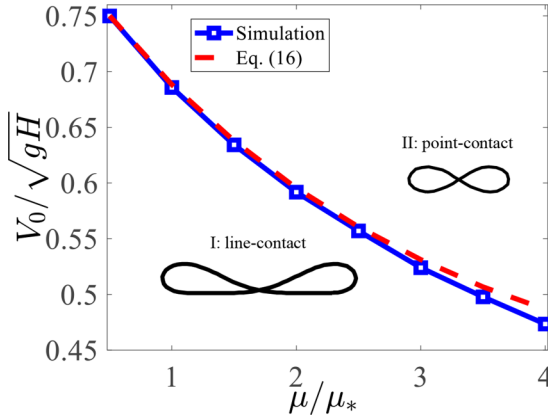
FIG. 8. Phase diagram of the folding morphology. The solid line with symbol represents the exact simulation results of V_c, and the dashed line represents the solution according to Eq. (16).

F. Phase diagram

Since the critical fold length below which the fold pattern changes from line contact to point contact equals $l_{f\_c} = 4.65l_c$, the corresponding critical velocity V_c can be identified based on the simulation results of l_f versus V_0 in Fig. 6. Figure 8 shows the phase diagram of the fold pattern. The solid line represents the exact simulation results of V_c, which separates the two different phases of folding morphology. We can also predict V_c by using the scaling law $l_f \sim 1/V_0$ [shown as Eq. (13)] and obtain

$$\frac{V_c}{\sqrt{gH}} = \frac{\varphi(\mu)}{4.65}. \tag{16}$$

The dashed line shown in Fig. 8 represents the prediction by the above equation. For low viscosity the prediction matches well the simulation, but it starts to deviate as viscosity increases, because as μ increases the viscous dissipation becomes significant, and the scaling law $l_f \sim 1/V_0$ ceases to be valid, which results in the deviation. Overall, the folding morphology transforms from line contact to point contact as the feeding velocity and viscosity increase.

The foregoing conclusions apply to falling sheets with properties similar to paper. The conclusions are not likely to apply for sheets where the viscous bending dissipation is comparable to the elastic bending energy.

IV. CONCLUSION

In this paper a one-dimensional particle dynamics model has been applied to investigate the periodic folding of a viscoelastic solid sheet fed from a specified height towards a rigid horizontal plane. The sheet is modeled as a series of discrete particles connected by Kelvin-Voigt-type viscoelastic solid elements, which can account for the large buckling deformation and the viscous dissipation. The folding process is associated with both bending and in-plane stretching viscous dissipations, since the extensibility of the sheet is considered in the current model. At a relatively low feeding velocity and low viscosity, the inertial effect and the viscous dissipations are negligible, and our model successfully reproduces the existing quasistatic results in this gravitational regime. As

the feeding velocity and the viscosity increase, the folding process changes significantly, and the "rolling back" motion of the sheet observed in the quasistatic case vanishes. Since the fold is closed faster with higher vertical feeding speed and the sheet expands slower horizontally at a higher viscosity, the fold length l_f is decreased. Upon further increasing V_0 the system enters into the inertial regime, where the kinetic energy becomes much higher than the gravitational potential. By balancing the kinetic energy and the elastic bending energy while neglecting the viscous dissipation, the fold length is found to be inversely proportional to the feeding velocity, i.e., $l_f \sim 1/V_0$, which matches very well the simulation results in the inertial regime. Furthermore, when V_0 exceeds a critical value V_c, the normalized fold height h_f/l_c starts decreasing, and the fold morphology transforms from line contact into point contact. Finally, a phase diagram for the fold morphology is constructed. The results presented in this work may provide some insights into the manufacturing process of paper and fabric sheets.

APPENDIX A: DERIVATION OF VISCOUS BENDING FORCE

Figure 9 shows a beam segment undergoing bending deformation by an angle of θ. During bending, viscous stresses are developed at the section in order to slow down the deformation process. For any point on the beam's section, viscous stress can be written in terms of dynamic viscosity (μ) and strain rate ($\dot{\epsilon}$) at that point of the section as

$$\sigma_v = \mu\dot{\epsilon} \tag{A1}$$
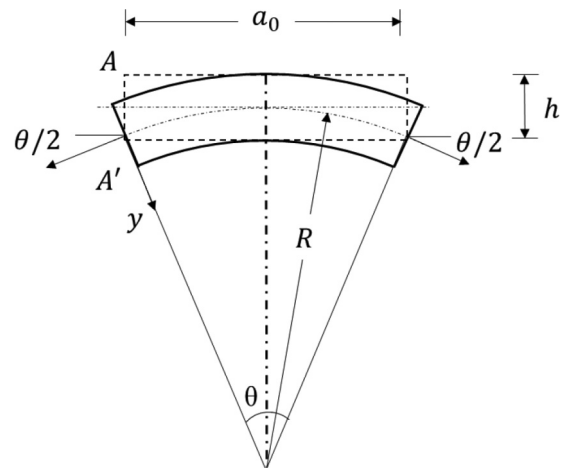
FIG. 9. Schematic of a beam segment of length a_0, width w, and thickness h undergoing bending deformation by an angle θ such that the section A deforms to A', the radius of curvature after deformation is R.
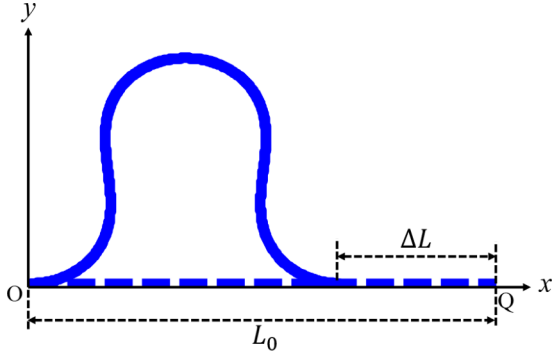
FIG. 10. Schematic of an elastica under axial load with clamping boundary condition before buckling (dashed line) and after buckling (solid line). O and Q are the endpoints, L_0 is the original length, and ΔL is the displacement of end point Q after deformation.

For a point on the section at a distance y from the neutral axis (positive direction of y is shown in Fig. 9), the axial strain can be written as

$$\epsilon = \frac{y}{R}. \tag{A2}$$

Hence the strain rate will be

$$\dot{\epsilon} = -\frac{y\dot{R}}{R^2}. \tag{A3}$$

Using inextensibility of the neutral axis, it can be shown that

$$\sigma_v = \mu \frac{y\dot{\theta}}{a_0}, \tag{A4}$$

where $\dot{\theta}$ is the rate of bending deformation of the segment. The viscous bending moment can be written as

$$M_v = \int_{-h/2}^{h/2} \sigma_v y w \, dy = \mu \frac{\dot{\theta}w}{a_0} \frac{h^3}{12}. \tag{A5}$$

Finally the viscous bending force can be calculated:

$$f_v = \frac{M_v}{a_0} = \frac{c_a \dot{\theta} h^2}{12 a_0}, \tag{A6}$$
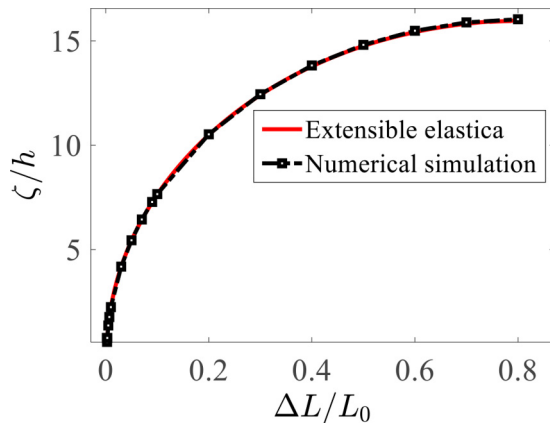
FIG. 11. Normalized deflection ζ/h vs normalized end displacement $\Delta L/L_0$. The solid line represents the solution of extensible elastica model obtained by shooting method, and the dashed line with open symbols represents the simulation results.
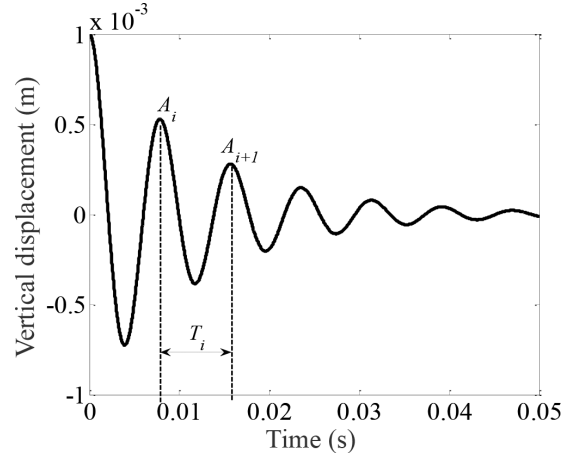
FIG. 12. Time response of the deflection of the mid-point of an excited simply supported beam.

where $c_a = \mu w h/a_0$ is the phenomenological damping coefficient.

APPENDIX B: ELASTIC MODEL VALIDATION

Consider a thin film under uniaxial load without substrate. It will buckle once the compressive strain exceeds the Euler strain. As the strain further increases, the self-contact of the film eventually occurs. The large buckling deformation of the film can be described by the extensible elastica model with the following governing equations [35,36]:

$$\frac{\partial x}{\partial s} = (1 + \varepsilon)\cos\theta, \tag{B1}$$

$$\frac{\partial y}{\partial s} = (1 + \varepsilon)\sin\theta, \tag{B2}$$

$$\frac{\partial M}{\partial s} = (1 + \varepsilon)(F_x \sin\theta - F_y \cos\theta), \tag{B3}$$

$$\frac{\partial \theta}{\partial s} = \frac{M}{EI}, \tag{B4}$$

$$\varepsilon = \frac{1}{EA}(F_x \cos\theta + F_y \sin\theta), \tag{B5}$$

where x and y are the coordinates, s is the length of the undeformed film measured from the endpoint O, shown in Fig. 10, θ is the rotation angle of the cross section, M is the bending moment, F_x and F_y are the internal forces, ε is the in-plane strain, $A = wh$ is the cross-sectional area, and $EI = Ewh^3/12$ is the bending stiffness. Here we consider a

TABLE II. Damped response comparison.

ν (m²/s)	Theory		Simulation	
	f_{d1} (Hz)	ζ_1	$f_{d1(sim)}$ (Hz)	ζ_1
0	128.3	0	128.2	0
10	128.2	0.0005	128.2	0.0005
2000	127.6	0.1007	127.6	0.1007
4000	125.6	0.2015	125.6	0.2014
8000	117.4	0.4029	117.6	0.4025

TABLE III. Beam properties.

Parameter	Value
Elastic modulus (E)	4 GPa
Density (ρ)	500 kg/m^3
Length (L)	1 m
Width (w)	0.1 m
Height (h)	0.1 m

TABLE IV. Convergence test ($\nu = 2000$ m^2/s).

No. of particles (N)	ζ_1(simulation)	ζ_1 (theory)
21	0.1005	
51	0.1007	0.1007
71	0.1007	

fixed-fixed boundary condition, which gives

$$x = 0, y = 0, \quad \theta = 0 \quad \text{at} \ s = 0 \ (\text{endpoint O}), \quad \text{(B6)}$$

$$x = L_0 - \Delta L, \quad y = 0, \quad \theta = 0 \quad \text{at} \ s = L_0 \ (\text{endpoint Q}), \quad \text{(B7)}$$

where L_0 is the undeformed length of the film and ΔL is the displacement of the endpoint Q. Equations (B1)–(B7) form a boundary value problem, which we can solve by shooting method. Next we compare our simulation results with the solutions given by the extensible elastica model.

In our simulation, the load is applied by controlling the displacement of the endpoint Q. The numerical damping coefficient is chosen as $\lambda = 0.001$ to help the system converge faster to the final equilibrium state for each given load. The length of the film is chosen as $L_0 = 40h$, and the film is discretized into 201 particles. Enough number of particles should be chosen so that the local bending satisfies $(\gamma_0 - \gamma_i) < 30°$. Under this condition the relative numerical error is less than 1% [30]. The fixed boundary condition is satisfied by imposing the y coordinates of the first two particles at each end of the film as zero. Figure 11 plots the maximum deflection of the film at equilibrium state under different load before self-contact occurs. Our numerical simulation results match very well the solutions given by the extensible elastica model.

APPENDIX C: VISCOUS MODEL VALIDATION

In this section, we validate the damping model adopted in this paper. A simply-supported beam has been excited in its first mode, and the time response at the midpoint of the beam is being monitored, which has been shown in Fig. 12. The first mode has been excited by giving an initial displacement of a half sinusoidal displacement profile to the beam. Using A_i and A_{i+1} to represent the peak values of the ith and $i + 1$-th peaks, the ith damping ratio can be calculated by the following equation:

$$\zeta_i = \frac{\ln \frac{A_i}{A_{i+1}}}{\sqrt{4\pi^2 + \left(\ln \frac{A_i}{A_{i+1}}\right)^2}}. \quad \text{(C1)}$$

Since the horizontal separation between those peaks represents the time period T_i, $1/T_i$ represents the damped frequency in Hz. Finally, the damping ratio and the frequency for different peaks are averaged to find a single value for the entire time response.

Table II shows the comparison of first mode damped frequencies (f_{d1}) and damping ratios (ζ_1) obtained by simulation with those from theory. In the simulations, the beam is discretized in 51 particles, and the kinematic viscosity is varied from 10 to 8000 m^2/s. The first row ($\nu = 0$) represents the undamped vibration frequency response. Beam properties used have been listed in Table III. The theoretical first mode damping ratio is calculated using $\zeta_1 = (\pi^2 \nu/2L^2)\sqrt{\rho E I/wh}$ [37], where symbols' definitions are consistent with those in Table III.

Table II indicates an almost exact match between the theory and the simulation, and the difference in some cases suggests the need for a finer discretization. Table IV shows the convergence test of our model. It suggests that our simulation results gradually converge to the theoretical value as the number of particles increases.

[1] M. Skorobogatiy and L. Mahadevan, Folding of viscous sheets and filaments, Europhys Lett. **52**, 532 (2000).

[2] N. M. Ribe, Periodic folding of viscous sheets, Phys. Rev. E **68**, 036305 (2003).

[3] N. M. Ribe, Bending and stretching of thin viscous sheets, J. Fluid Mech. **433**, 135 (2001).

[4] L. Mahadevan and J. B. Keller, Periodic folding of thin sheets, SIAM Rev. **41**, 115 (1999).

[5] J. O. Cruickshank, Low-Reynolds-number instabilities in stagnating jet flows, J. Fluid Mech. **193**, 111 (1988).

[6] D. W. Lloyd, W. J. Shanahan, and M. Konopasek, The folding of heavy fabric sheets, Int. J. Mech. Sci. **20**, 521 (1978).

[7] T. G. Sano, T. Yamaguchi, and H. Wada, Slip Morphology of Elastic Strips on Frictional Rigid Substrates, Phys. Rev. Lett. **118**, 178001 (2017).

[8] P. J. Hudleston and S. H. Treagus, Information from folds: A review, J. Struct. Geol. **32**, 2042 (2010).

[9] J. R. A. Pearson, *Mechanics of Polymer Processing* (Elsevier, London, 1985).

[10] L. Mahadevan and J. B. Keller, Coiling of flexible ropes, Proc. R. Soc. Lond. A **452**, 1679 (1996).

[11] L. Mahadevan, W. S. Ryu, and A. D. Samuel, Fluid 'rope trick' investigated, Nature (London) **392**, 140 (1998).

[12] N. M. Ribe, M. Habibi, and D. Bonn, Liquid rope coiling, Annu. Rev. Fluid Mech. **44**, 249 (2012).

[13] N. M. Ribe, Coiling of viscous jets, Proc. R. Soc. London Ser. A **460**, 3223 (2004).

[14] M. Habibi, M. Maleki, R. Golestanian, N. M. Ribe, and D. Bonn, Dynamics of liquid rope coiling, Phys. Rev. E **74**, 066306 (2006).

[15] M. Habibi, N. M. Ribe, and D. Bonn, Coiling of Elastic Ropes, Phys. Rev. Lett. **99**, 154302 (2007).

[16] M. K. Jawed, F. Da, J. Joo, E. Grinspun, and P. M. Reis, Coiling of elastic rods on rigid substrates, Proc. Natl. Acad. Sci. USA **111**, 14663 (2014).

[17] M. K. Jawed, P. T. Brun, and P. M. Reis, A geometric model for the coiling of an elastic rod deployed onto a moving substrate, J. Appl. Mech. **82**, 121007 (2015).

[18] M. K. Jawed and P. M. Reis, Pattern morphology in the elastic sewing machine, Extreme Mech. Lett. **1**, 76 (2014).

[19] P. T. Brun, B. Audoly, N. M. Ribe, T. S. Eaves, and J. R. Lister, Liquid Ropes: A Geometrical Model for Thin Viscous Jet Instabilities, Phys. Rev. Lett. **114**, 174501 (2015).

[20] M. Habibi, J. Najafi, and N. M. Ribe, Pattern formation in a thread falling onto a moving belt: An "elastic sewing machine," Phys. Rev. E **84**, 016219 (2011).

[21] M. J. Blount, Bending and buckling of a falling viscous thread, Doctoral thesis, Cambridge University, 2010.

[22] M. J. Blount and J. R. Lister, The asymptotic structure of a slender dragged viscous thread, J. Fluid Mech. **674**, 489 (2011).

[23] M. Alava and K. Niskanen, The physics of paper, Rep. Prog. Phys. **69**, 669 (2006).

[24] W. G. Hoover, C. G. Hoover, O. Kum, V. M. Castillo, H. A. Posch, and S. Hess, *Smooth Particle Applied Mechanics* (World Scientific, Singapore, 2006).

[25] A. A. Munjiza, E. E. Knight, and E. Rougier, *Computational Mechanics of Discontinua* (John Wiley & Sons, Chichester, 2011).

[26] J. Persson and P. Isaksson, A particle-based method for mechanical analyses of planar fiber-based materials, Int. J. Numer. Methods Eng. **93**, 1216 (2013).

[27] C. Batty, A. Uribe, B. Audoly, and E. Grinspun, Discrete viscous sheets, ACM Tran. Graphics **31**, 113 (2012).

[28] M. Bergou, M. Wardetzky, S. Robinson, B. Audoly, and E. Grinspun, Discrete elastic rods, ACM Tran. Graphics **27**, 63:1 (2008).

[29] S. Li and W. K. Liu, Meshfree and particle methods and their applications, Appl. Mech. Rev. **55**, 1 (2002).

[30] S. Edvardsson and T. Uesaka, System dynamics of the open-draw with web adhesion: Particle approach, J. Appl. Mech. **77**, 021009 (2010).

[31] K. Pan, A. S. Phani, and S. Green, Particle dynamics modeling of the creping process in tissue making, J. Manuf. Sci. Eng. **140**, 071003 (2018).

[32] K. Pan, R. Das, A. S. Phani, and S. Green, An elastoplastic creping model for tissue manufacturing, Int. J. Solids Struct. **165**, 23 (2019).

[33] K. Marynowski and T. Kapitaniak, Kelvin–Voigt versus Bürgers internal damping in modeling of axially moving viscoelastic web, Int. J. Non Linear Mech. **37**, 1147 (2002).

[34] G. Domokos and P. Holmes, Euler's problem, Euler's method, and the standard map; or, the discrete charm of buckling, J. Nonlinear Sci. **3**, 109 (1993).

[35] E. Reissner, On one-dimensional finite-strain beam theory: The plane problem, Z. Angew. Math Phys. **23**, 795 (1972).

[36] J. E. Flaherty and J. B. Keller, Contact problems involving a buckled elastica, SIAM J. Appl. Math. **24**, 215 (1973).

[37] P. Hagedorn and A. DasGupta, *Vibrations and Waves in Continuous Mechanical Systems* (Wiley, Chichester, 2007), pp. 113–120.